

Tetsuji Yamada*

Yamada Science & Art Corporation, Santa Fe, New Mexico

1. INTRODUCTION

Considerable interest exists in understanding airflows and dispersion of airborne materials in an urban environment. Urban areas are known to be warmer (urban heat islands) than surrounding rural areas due to anthropogenic heat releases and modifications of soil surfaces by concrete structures. Buildings block airflows and airflows are accelerated in the building corridors. Urban areas contribute significantly to the modification of microclimate.

Urban areas present unique environmental problems. Automobile emissions and accidental and terrorist releases of toxic materials in an urban environment result in a potentially serious consequence due to high population density.

Several approaches were considered to incorporate urban effects into numerical models. A first approach is to treat buildings as roughness elements. This method is appropriate only when interest is limited in the layer above the building height. It is not, however, appropriate if the interest includes airflow in the street level, which is the case discussed here.

A second approach is to treat buildings in a fashion similar to tall tree canopies (Uno et al., 1989; Kondo et al., 1998; Ooka et al., 2004). Buildings induce drag to the airflows. Building clusters are parameterized in terms of the ratios of building volume to the grid volume. This approach is useful in the atmospheric models where the horizontal grid size is too large to resolve each building.

A third approach is to simulate airflows around individual buildings. This approach is ideal and common in the computational fluid dynamics (CFD) community, but computation time could be extensive because grid spacing is small.

A typical grid size for a CFD model is a few meters while a typical grid size for an atmospheric model is a few kilometers. In other words, a difference of three orders of magnitude exists in grid size between a CFD model and an atmospheric model.

In addition, CFD models typically provide steady state solutions while atmospheric models deal with diurnal variations. Atmospheric models include water vapor, clouds, and rain, but CFD models do not. Thus, not only grid size, but also model physics are quite different between the CFD and atmospheric models.

Recently, there have been some efforts in fusing the CFD and atmospheric model capabilities to address effects on airflows from building to terrain scales (Pielke et al., 1997; Gross., 2000; Yamada, 2004). This is what is required to simulate airflows over the urban areas in complex terrain and/or in coastal areas.

This paper discusses how an atmospheric model was improved and used to simulate diurnal variations of air flows around buildings.

2. MODEL EQUATIONS

The basic equations for mean wind, temperature, mixing ratio of water vapor, and turbulence are similar to those used by Yamada and Bunker (1988).

In order to accurately treat surface boundary conditions, a terrain-following vertical coordinate system is used:

$$z^* = \bar{H} \frac{z - z_g}{H - z_g}, \quad (1)$$

where z^* and z are the transformed and Cartesian vertical coordinates, respectively; z_g is ground elevation; \bar{H} is the top of the computation domain in the z^* coordinate and H is the corresponding height in the z coordinate.

*Corresponding author address: Tetsuji Yamada, Yamada Science & Art Corporation, Santa Fe, New Mexico 87506; e-mail: ysausa@ysasoft.com.

The governing equations following the coordinate transformation are

$$\begin{aligned} \frac{DU}{Dt} &= f(V - V_g) + g \frac{\bar{H} - z^*}{\bar{H}} \left(1 - \frac{\langle \Theta_v \rangle}{\Theta_v} \right) \frac{\partial z_g}{\partial x} \\ &+ \frac{\partial}{\partial x} \left(K_x \frac{\partial U}{\partial x} \right) + \frac{\partial}{\partial y} \left(K_{xy} \frac{\partial U}{\partial y} \right) + \frac{\bar{H}}{H - z_g} \frac{\partial}{\partial z^*} (-\overline{uw}) \\ &- \eta C_d a(z) U |U| + G(U_o - U), \end{aligned} \quad (2)$$

$$\begin{aligned} \frac{DV}{Dt} &= f(U - U_g) + g \frac{\bar{H} - z^*}{\bar{H}} \left(1 - \frac{\langle \Theta_v \rangle}{\Theta_v} \right) \frac{\partial z_g}{\partial y} \\ &+ \frac{\partial}{\partial x} \left(K_{xy} \frac{\partial V}{\partial x} \right) + \frac{\partial}{\partial y} \left(K_y \frac{\partial V}{\partial y} \right) + \frac{\bar{H}}{H - z_g} \frac{\partial}{\partial z^*} (-\overline{vw}) \\ &- \eta C_d a(z) V |V| + G(V_o - V), \end{aligned} \quad (3)$$

$$\begin{aligned} \frac{DW}{Dt} &= -\frac{1}{\rho} \frac{\partial P}{\partial z} - g + \frac{\partial}{\partial z} (-\overline{wv}) + \frac{\partial}{\partial x} \left(K_{zx} \frac{\partial W}{\partial x} \right) \\ &+ \frac{\partial}{\partial y} \left(K_{yz} \frac{\partial W}{\partial y} \right) - \eta C_d a(z) W |W| + G(W_o - W), \end{aligned} \quad (4)$$

$$\frac{\partial U}{\partial x} + \frac{\partial V}{\partial y} + \frac{\partial W^*}{\partial z^*} - \frac{1}{H - z_g} \left(U \frac{\partial z_g}{\partial x} + V \frac{\partial z_g}{\partial y} \right) = 0, \quad (5)$$

where

$$W^* \equiv \frac{\bar{H}}{H - z_g} W + \frac{z^* - \bar{H}}{H - z_g} \left(U \frac{\partial z_g}{\partial x} + V \frac{\partial z_g}{\partial y} \right), \quad (6)$$

and

$$\frac{D(\cdot)}{Dt} \equiv \frac{\partial(\cdot)}{\partial t} + U \frac{\partial(\cdot)}{\partial x} + V \frac{\partial(\cdot)}{\partial y} + W^* \frac{\partial(\cdot)}{\partial z^*}. \quad (7)$$

In the above expressions, U, V, and W are ensemble averaged velocity components in x, y, and z directions, respectively, $\langle \cdot \rangle$ indicates an average over a horizontal surface. The second terms on the right-hand side of eqs. (2) and (3) indicate the effects of ground slope, which are resulted from the coordinate transformation. C_d a drag coefficient for a forest canopy, $a(z)$ the plant

area density, η a fraction of the area covered by trees $0 \leq \eta \leq 1$. The last terms on the right hand sides of eqs. (2), (3), and (4) are used in nudging the variables toward observed or large-scale prediction values (U_o , V_o , W_o). G is a nudging coefficient whose magnitude is in the order of Coriolis parameter.

For simplicity, H is specified as

$$H = \bar{H} + z_{g \max} \quad (8)$$

where $z_{g \max}$ is the max height of ground elevation in the study area.

The geostrophic winds U_g and V_g are computed from

$$\begin{aligned} fU_g &\equiv fU_g(\bar{H}) \frac{\langle \Theta_v \rangle}{\langle \Theta_v(\bar{H}) \rangle} + g \frac{H - z_g}{\bar{H}} \\ &\times \int_{z^*}^{\bar{H}} \frac{1}{\langle \Theta_v \rangle} \frac{\partial \Delta \Theta_v}{\partial y} dz' - \frac{g}{H} \frac{\partial z_g}{\partial y} \int_{z^*}^{\bar{H}} \frac{\Delta \Theta_v}{\langle \Theta_v \rangle} dz', \end{aligned} \quad (9)$$

and

$$\begin{aligned} fV_g &\equiv fV_g(\bar{H}) \frac{\langle \Theta_v \rangle}{\langle \Theta_v(\bar{H}) \rangle} - g \frac{H - z_g}{\bar{H}} \\ &\times \int_{z^*}^{\bar{H}} \frac{1}{\langle \Theta_v \rangle} \frac{\partial \Delta \Theta_v}{\partial x} dz' + \frac{g}{H} \frac{\partial z_g}{\partial x} \int_{z^*}^{\bar{H}} \frac{\Delta \Theta_v}{\langle \Theta_v \rangle} dz', \end{aligned} \quad (10)$$

where $\Delta \Theta_v \equiv \Theta_v - \langle \Theta_v \rangle$, and the abbreviated symbols $U_g(\bar{H}) \equiv U_g(x, y, \bar{H}, t)$, $V_g(\bar{H}) \equiv V_g(x, y, \bar{H}, t)$, etc., are used.

A turbulence kinetic energy equation is given by

$$\begin{aligned} \frac{D}{Dt} \left(\frac{q^2}{2} \right) &= \frac{\partial}{\partial x} \left[K_x \frac{\partial}{\partial x} \left(\frac{q^2}{2} \right) \right] + \frac{\partial}{\partial y} \left[K_y \frac{\partial}{\partial y} \left(\frac{q^2}{2} \right) \right] \\ &+ \left(\frac{\bar{H}}{H - z_g} \right)^2 \frac{\partial}{\partial z^*} \left[q l S_q \frac{\partial}{\partial z^*} \left(\frac{q^2}{2} \right) \right] \end{aligned}$$

$$\begin{aligned}
& -\frac{\bar{H}}{H-z_g} \left(\overline{uw} \frac{\partial U}{\partial z^*} + \overline{vw} \frac{\partial V}{\partial z^*} \right) \\
& + \beta \bar{g} \overline{w\theta_v} - \frac{q^3}{B_1 l} + \eta C_d a(z) \left[U^2 + V^2 + W^2 \right]^{3/2} \quad (11)
\end{aligned}$$

and a turbulence length scale l is obtained from

$$\begin{aligned}
\frac{D}{Dt} (q^2 l) &= \frac{\partial}{\partial x} \left[K_x \frac{\partial}{\partial x} (q^2 l) \right] + \frac{\partial}{\partial y} \left[K_y \frac{\partial}{\partial y} (q^2 l) \right] \\
& + \left(\frac{\bar{H}}{H-z_g} \right)^2 \frac{\partial}{\partial z^*} \left[q l S_l \frac{\partial}{\partial z^*} (q^2 l) \right] \\
& + l F_1 \left[\frac{\bar{H}}{H-z_g} \left(-\overline{uw} \frac{\partial U}{\partial z^*} - \overline{vw} \frac{\partial V}{\partial z^*} \right) + \beta \bar{g} \overline{w\theta_v} \right] \\
& - \frac{q^3}{B_1} \left[1 + F_2 \left(\frac{1}{kz} \right)^2 \right] \\
& + 2\eta C_d a(z) l \left[U^2 + V^2 + W^2 \right]^{3/2} \quad (12)
\end{aligned}$$

where $q^2 = \overline{u^2} + \overline{v^2} + \overline{w^2}$ is twice the turbulence kinetic energy, $\overline{w\theta_v}$ turbulence heat flux, θ_v the fluctuation part of virtual potential temperature, and $(F_1, F_2, S_q, S_l, \text{ and } B_1) = (1.8, 1.33, 0.2, 0.2, \text{ and } 16.6)$ empirical constants determined from laboratory experiments. The last terms on the right hand sides of eqs. (11) and (12) are turbulence production due to tree canopy.

The internal heat energy equation is written as

$$\begin{aligned}
\frac{D\Theta}{Dt} &= \frac{\partial}{\partial x} \left[K_x \frac{\partial \Theta}{\partial x} \right] + \frac{\partial}{\partial y} \left[K_y \frac{\partial \Theta}{\partial y} \right] \\
& + \frac{\bar{H}}{H-z_g} \left[\frac{\partial}{\partial z^*} (-\overline{w\theta}) \right]. \quad (13)
\end{aligned}$$

A conservation equation for mixing ratio of water vapor is given by

$$\begin{aligned}
\frac{DQ_v}{Dt} &= \frac{\partial}{\partial x} \left[K_x \frac{\partial Q_v}{\partial x} \right] + \frac{\partial}{\partial y} \left[K_y \frac{\partial Q_v}{\partial y} \right] \\
& + \frac{\bar{H}}{H-z_g} \frac{\partial}{\partial z^*} (-\overline{wq_v}). \quad (14)
\end{aligned}$$

The turbulent fluxes in eqs. (2), (3), (11), (12), (13), and (14) are obtained from simplified second-moment turbulence-closure equations:

$$(\overline{uw}, \overline{vw}) = -lq\tilde{S}_M \left[\frac{\partial U}{\partial z}, \frac{\partial V}{\partial z} \right] \quad (15a, b)$$

$$\overline{ww} = \left(\gamma - 6A_1 \frac{R_f}{B_1} (1 - R_f) \right) q^2, \quad (15c)$$

where $\gamma = 0.222$, $A_1 = 0.92$, $B_1 = 16.6$, $R_f < R_{fc}$, $R_{fc} = 0.19$

$$(\overline{w\theta}, \overline{wq_v}) = -\alpha lq\tilde{S}_M \left[\frac{\partial \Theta}{\partial z}, \frac{\partial Q_v}{\partial z} \right] \quad (16a, b)$$

where \tilde{S}_M and α are functions of the flux Richardson number, and α ($\equiv K_H/K_M$ where K_H is an eddy diffusivity coefficient and K_M is an eddy viscosity coefficient) is the reciprocal of the turbulent Prandtl number.

The expressions for \tilde{S}_M and α were obtained from the level 2 model of Mellor and Yamada (1974) where temporal and spatial derivatives in eq. (11) are neglected. The readers are referred to Yamada (1975) for further discussions of the level 2 model equations. The final expressions for \tilde{S}_M and α are given in Yamada (1983) and are not repeated here. The turbulent flux in the vertical direction (15c) was obtained from the level 2 model equations.

2.2. Pressure Velocity Adjustments

The hydrostatic equilibrium is a good approximation in the atmosphere. On the other hand, airflows around buildings are not in the hydrostatic equilibrium. Pressure variations are generated by changes in wind speeds, and the resulted pressure gradients subsequently affect wind distributions. We adopted HSMAC method (Hirt and Cox, 1972) for pressure computation

because the method is simple yet efficient. The method is equivalent in solving a Poisson equation, which is commonly used in non-hydrostatic atmospheric models.

The continuity equation is

$$D = \frac{\partial U}{\partial x} + \frac{\partial V}{\partial y} + \frac{\partial W}{\partial z} = 0. \quad (16)$$

From equation of motion, the following relation is obtained between pressure adjustment term and the wind divergence term (Hirt and Cox, 1972):

$$\Delta^l P_{i,j,k} = - \frac{\rho_{i,j,k}}{2\Delta t \left(\frac{1}{\Delta x^2} + \frac{1}{\Delta y^2} + \frac{1}{\Delta z^2} \right)} \left\{ \frac{\partial U}{\partial x} + \frac{\partial V}{\partial y} + \frac{\partial W}{\partial z} \right\} \quad (17)$$

where $\rho_{i,j,k}$ is the air density. $\Delta x, \Delta y,$ and Δz are grid sizes in the x, y, and z directions, respectively.

If the divergence term were not zero, wind components are adjusted, for example,

$$U_{i,j,k}^{l+1} = U_{i,j,k}^l + \frac{1}{\rho} \frac{\Delta t}{\Delta x} \Delta^l P_{i,j,k} \quad (18)$$

$$U_{i-1,j,k}^{l+1} = U_{i-1,j,k}^l - \frac{1}{\rho} \frac{\Delta t}{\Delta x} \Delta^l P_{i,j,k} \quad (19)$$

If $\Delta^l P_{i,j,k}$ is positive, $U_{i,j,k}^l$ will be accelerated and $U_{i-1,j,k}^l$ will be decelerated. Similar adjustments are made for wind components V and W. Iterations continue until the divergence term becomes less than a specified value.

3. EXAMPLES OF SIMULATIONS

Two cases were considered to illustrate the thermal effects of building walls and rooftops on the air flows. In Case1, steady state was assumed and the building wall and rooftop temperatures were forced to be the same as the air temperatures adjacent to the walls and rooftops. In other words, only the dynamic effects of buildings were considered.

Case 2 was for the unsteady steady case where the sun's zenith angle varied with time. For example, west walls received more heat energy from the sun during the late afternoon than the east walls. During the night time, building surfaces were cooled by radiation and the wall temperatures became lower than the air temperatures adjacent to the walls.

The computation domain was 200 m x 200 m in the horizontal directions and 500 m in the vertical direction. Horizontal grid spacing was 4 m. Vertical grid spacing was 4 m for the first 15 levels and increased gradually with height. There were 30 levels in the vertical direction.

Two buildings were placed along the centerline of the computational domain. Each building was 32 m (W) x 32 m (D) x 30 m (H). Winds were initially westerly and 5 m/s everywhere except in the surface layer where logarithmic profiles were assumed. Boundary conditions were imposed by a nudging method so that winds were westerly and 5 m/s in the layers higher than 200 m above the ground.

The lapse rate of potential temperature profiles were initially 1 degree/1000 m in the layer less than 200 in height and 3 degrees/1000 m in the layers higher than 200 m above the ground. Boundary conditions were imposed by a nudging method at the inflow boundary and the layers higher than 200 m above the ground.

The temperatures in the soil layer were obtained by numerically integrating a one-dimensional heat conduction equation (Yamada and Bunker, 1988). Appropriate boundary conditions for the soil temperature equation were the heat energy balance at the ground and specification of the soil temperature at 30 cm below the surface, where temperature was constant during the integration period. The surface heat energy balance consists of solar radiation, long-wave radiation, sensible heat, latent heat, and heat fluxes into the soil layers.

Wall and rooftop temperatures of buildings were determined similarly by numerically integrating a one-dimensional heat conduction equation in the direction perpendicular to the walls and rooftops. Boundary conditions were the heat energy balance at the surfaces exposed to the atmosphere and indoor wall and ceiling temperatures (25 degrees C was assumed).

Multiple reflections of short- and long-wave radiation at building walls play important role in determining the heat energy balance at building surfaces. For a small number of buildings considered in this study, however, complex reflections of short- and long-wave radiation were not considered. This should not affect seriously the present objective, which was to examine relative importance of heating and cooling of the building walls and rooftops on the air circulations around two buildings.

Fig. 1 shows the modeled wind distributions for Case 1 in the vertical cross section along the centerline of the computational domain. Wind speed were normalized in order to show wind directions clearly in the cavity between the two buildings where wind speeds were less than 2 m/s.

In Case 1, building wall and rooftop temperatures were forced to be the same as the air temperatures adjacent to the walls and rooftops.

Upward motion and separation of air flows were obtained along the leading edge of the first building. Separation of air flows and recirculation were seen in the lee ward of the buildings. The modeled airflow circulations were similar to those observed in wind tunnel experiments where the building temperatures were the same as the air temperatures.

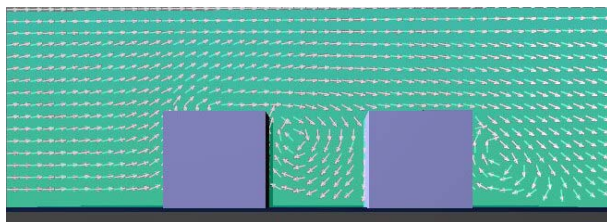


Figure 1: The modeled wind distributions in the vertical cross section along the centerline of the computational domain (steady state)

Figure 2 shows the modeled air flows at 2 p.m. in the vertical cross section along the centerline of the computational domain. Building wall and rooftop temperatures were computed by solving one-dimensional heat conduction equations in the direction normal to the surfaces. Boundary conditions were the heat energy balance at the outer surfaces and specified temperature at the inner surfaces.

Temperature distributions are shown in different colors whose numerical values are defined in the insertion.

Air circulations in the cavity between the two buildings for Case 2 were quite different from those for Case 1. Upward motions were observed along both the west and east walls.

Throughout the discussions the “east” and “west” walls refer to the east and west side walls of each building, but not to the east and west side walls of the cavity. In Fig. 2, the rotation of air flows was absent in the cavity between the two buildings.

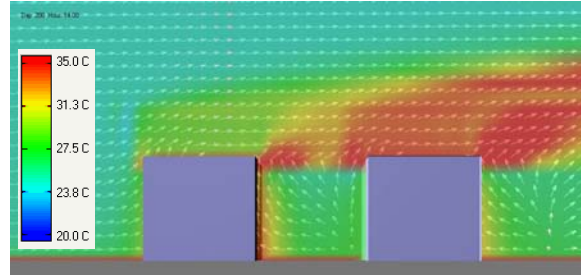


Figure 2: The modeled wind and temperature distributions at 2 p.m. in the vertical cross section along the centerline of the computational domain. Temperature distributions are shown in colors whose numerical values are shown in the insert.

Figure 3 is the same as for Fig. 2 except at 7 p.m. East walls started cooling by radiation and wall temperatures became lower than the air temperatures adjacent to the walls. Downward motion developed along the west walls, but upward motion remained along the east walls where wall temperatures were still significantly higher than the air temperatures.

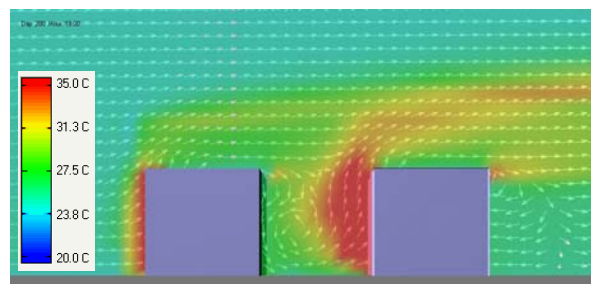


Figure 3: Same as for Fig.2 except at 7 p.m.

Consequently, the air circulations between the two buildings were in the counter clockwise direction. This direction of rotation was opposite to that for Case 1 (Fig. 1) where wall and rooftop temperatures were the same as for the air temperatures.

Dynamic pressures increased at the windward walls since kinetic energy of wind was converted into dynamic pressures (Bernoulli equation). On the other hand, dynamic pressures decreased at the leeward walls since dynamic pressures were converted into kinetic energy of winds. The lower dynamic pressures behind the first building resulted in the clockwise rotation. This is why the rotation direction for Case 1 was the same as in the approaching flow direction (Fig. 1).

When wall temperatures were higher than the air temperatures at the same height, hydrostatic pressure gradients developed in the horizontal direction, which moved air toward heated wall. Convergence of air flows resulted in upward motion along the heated wall due to the mass conservation constraint. When wall temperatures were lower than the air temperatures at the same height, on the other hand, downward motion developed along the cold walls.

If dynamic pressures were dominant, then clockwise rotation was the result in the cavity between the two buildings. If hydrostatic pressures were dominant, then counter clockwise rotation developed. Although pressure gradients were important forcing in the equations of motion, pressure distributions alone could not determine the airflow distributions. However, the above analysis appears to be a valid qualitative interpretation.

Figure 4 is the same as for Fig. 2 except at 1 a.m. in the following morning. East wall temperatures of the first building were significantly lower than the air temperatures adjacent to the wall, but west wall temperatures of the second building still remained higher than the air temperatures. The area of upward motion along the west wall of the second building decreased and the center of counter clockwise rotation in the cavity moved toward the second building.

On the other hand, the area of downward motion increased significantly along the east walls. The downward motion reached the ground and spread horizontally as shown in Fig. 5.

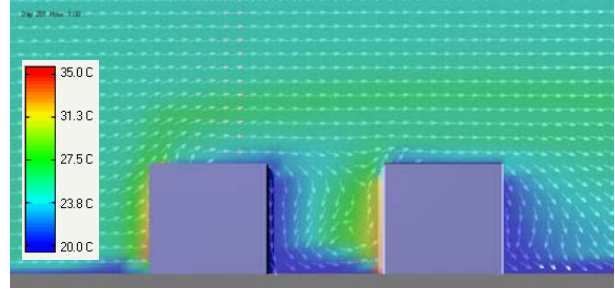


Figure 4: Same as for Fig. 2 except at 7 p.m.

Fig. 5 shows the wind distributions in the horizontal cross section at 2 m above the ground at 1 a.m. The downward motion along building walls transported cold air down to the ground. The cold air spills are indicated by the areas in dark blue. Small areas in red color indicate that the west walls are still warm.

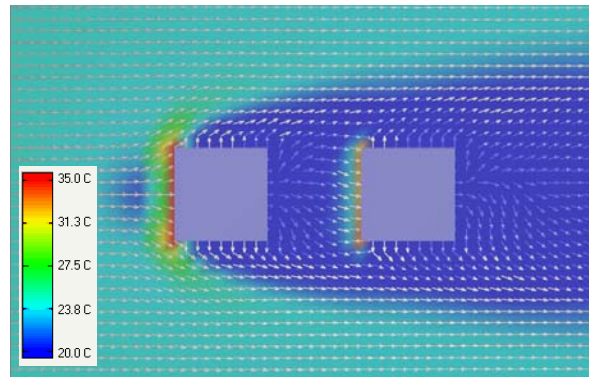


Figure 5: The modeled wind and temperature distributions at 1 a.m. in the horizontal cross section at 2 m above the ground

Figure 6 is the same as for Fig. 2 except at 2:50 a.m. Wall and rooftop temperatures continued to decrease with time due to radiation cooling. Upward motion along the west wall of the second building (Fig. 4) changed to the downward motion (Fig. 6).

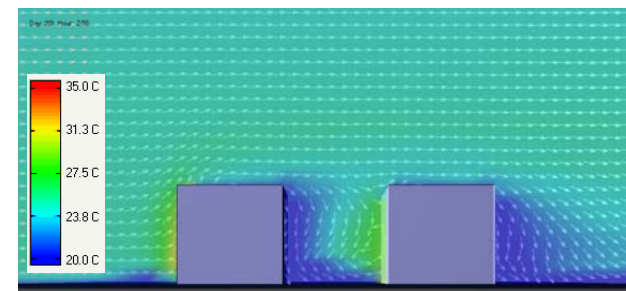


Figure 6: Same as for Fig. 2 except at 2:50 a.m.

SUMMARY

Numerical simulations were conducted to understand how the air flows around buildings were affected by heating and cooling of building walls and rooftops by solar radiation.

Two buildings were placed along the centerline of a computational domain of 200 m x 200 m x 500 m (vertical). Each building was 32 m (W) x 32 m (D) x 30 m (H).

Two cases were considered: Case 1 was for the steady state where wall and rooftop temperatures were the same as the air temperatures adjacent to the walls and rooftops. Case 1 represented the conditions encountered in wind tunnel experiments or CFD simulations where thermal effects of buildings were not considered.

Case 2 was for the unsteady case where sun's zenith angle varied with time. For example, west walls were heated most during late afternoon by the sun in comparison with other walls. Walls and rooftops were cooled by radiation during the nocturnal period and wall and rooftop temperatures became significantly lower than the air temperatures adjacent to the walls and rooftops.

All simulations were conducted in three-dimensional in space, but wind distributions in the vertical cross section along the centerline of the computational domain were used for comparisons of model results. The modeled air flows around building were significantly different for Case 1 (steady state) and Case 2 (unsteady state).

For Case1, the modeled air flows in the cavity between the two buildings rotated in clockwise direction. This agreed with the wind tunnel measurements and CFD simulations where thermal effects of buildings were not considered.

For Case2, the modeled air flows in the cavity varied considerably with time depending on the temperatures of the east and west walls and their differences from the air temperatures in the cavity. For example, rotation motion was absent in the cavity at 2 p.m. Upward air flows were dominant along both the east and west walls.

Downward motion developed by 7 p.m. as the east walls cooled by radiation and air flows in the cavity rotated in counter clockwise direction. This direction was opposite to that obtained in the steady state case.

Wall and rooftop temperature variations in time and space were in agreement qualitatively with limited number of measurements reported, mostly in architectural research community. Very few measurements of air flows in an urban canyon are available. Corresponding measurements during the nocturnal period are even more limited.

The present study suggested that heating and cooling of walls and rooftops by solar radiation significantly influenced the airflows around buildings in an urban environment.

REFERENCES

Gross, G., 2000, FITNAH (Flow over Irregular Terrain with Natural and Anthropogenic Heat sources), Short Course on Mesoscale Atmospheric Modeling by Original Model Developers, Long Beach, California, 9 January 2000, American Met. Soc.

Hirt, C.W., and J. L. Cox, 1972: Calculating Three-Dimensional Flows around Structures and over Rough Terrain. *J. of Computational Phys.*, **10**, 324-340.

Kondo, H., Y. Genchi, Y. Kikegawa, Y. Ohashi, H. Yoshikado and H. Komiyama, 2005, Development of a Multi-Layer Urban Canopy Model for the Analyses of Energy Consumption in a Big City; Structure of the Urban Canopy Model Performance, *Boundary Layer Met.*, (in press).

Mellor, G. L., and T. Yamada, 1974, A Hierarchy of Turbulence Closure Models for Planetary Boundary Layers. *J. of Atmos. Sci.*, **31**, 1791-1806.

Ooka, R., K. Hayama, S. Murakami, and H. Kondo, 2004, Study on Urban Heat Islands in Tokyo Metropolitan Area Using a Meteorological Mesoscale Model Incorporating an Urban Canopy Model, Fifth Symposium on the Urban Environment, Vancouver, British Columbia, Canada, 23-26, August 2004, American Met. Soc.

Pielke, R. Sr. and M. Nicholls, 1997, Use of Meteorological Models in Computational Wind Engineering, *J. Wind Engineering and Indust. Aerodynamics* **67&68**, 363-372.

Uno, I., H. Ueda and S. Wakamatsu, 1989, Numerical Modeling of the Nocturnal Urban Boundary Layer, *Boundary Layer Met.*, **49**, 77-98.

Yamada, T., 1975, The Critical Richardson Number and the Ratio of the Eddy Transport Coefficients Obtained from a Turbulence Closure Model. *J. of Atmos. Sci.*, **32**, 926-933.

Yamada, T., 1983, Simulations of Nocturnal Drainage Flows by a q^2 Turbulence Closure Model. *J. of Atmos. Sci.*, **40**, 91-106.

Yamada, T., 2004, Merging CFD and Atmospheric Modeling Capabilities to Simulate Airflows and Dispersion in Urban Areas, *Computational Fluid Dynamics Journal*, 13(2):**47**, 329-341.

Yamada, T., and S. Bunker, 1988, Development of a Nested Grid, Second Moment Turbulence Closure Model and Application to the 1982 ASCOT Brush Creek Data Simulation. *J. of Applied Meteorology*, **27**, 562-578.